2016 IEEE/RSJ International Conference on Robotics and Automation (ICRA)
May 16-21, 2016, Stockholm, Sweden.

Snap-On Robotic Wrist Module for Enhanced Dexterity in Endoscopic Surgery*

Joshua Gafford, *Student Member, IEEE,* Tommaso Ranzani, Sheila Russo, Dr. Hiroyuki Aihara, Dr. Christopher Thompson, Robert Wood, *Member, IEEE,* Conor Walsh, *Member, IEEE*

***Abstract*—Burgeoning transendoscopic procedures, such as endoscopic submucosal dissection (ESD), provide a promising means of treating early-stage gastric neoplasia in a minimally-invasive way. However, the remote locations of these lesions, coupled with their origination in the submucosal layers of the gastrointestinal tract, often lead to extreme technical, cognitive and ergonomic challenges which combat the widespread applicability and adoption of these techniques. Among these challenges is achieving the *in vivo* dexterity required to retract and dissect tissue. By leveraging workspace and force data obtained through clinical studies, we developed a modular, disposable, distally-mounted actuator (an 'active endcap') that can augment an endoscopist's distal dexterity in ways that are not achievable with the endoscope's built-in degrees-of-freedom. The device consists of a flexible articulating 'exoskeleton' manufactured via printed-circuit MEMS (PCMEMS) which engages and deflects electrosurgical tools that are passed through the endoscopic working channel. Embedded proprioceptive sensing is implemented on-board using distributed LED/phototransistor pairs and the principle of light intensity modulation (LIM). The distal degree-of-freedom is actuated using shape memory alloy (SMA) technology, and the actuation transmission system is fully contained within a 1-inch-long end cap that can be mounted on the distal end of the endoscope, thereby obviating the need for a mechanical connection to a proximal source. Proof-of-concept tests demonstrate that the actuator adds over 50 degrees of distal articulation to existing tools and can generate 450 mN of lateral force which has been clinically determined to be sufficient for performing circumferential incisions in ESD.**

I. Introduction

Innovation in robotic surgery is seeing a paradigm shift from rigid, teleoperative serial manipulators to flexible co-robotic tools capable of accessing remote locations inside the body [1]–[5]. This paradigm shift is concurrent with a desire to perform 'scarless' surgery through natural orifices to substantially reduce morbidity and recovery. While a number of systems have demonstrated unparalleled dexterity in navigating the body's tortuous anatomy, limited sophistication in end-effector design has severely impeded the therapeutic applications of these systems. To usher in the next generation of therapeutic endoscopic tools, it is of paramount importance to develop sophisticated end-effector morphologies that can extend the capabilities of these systems.

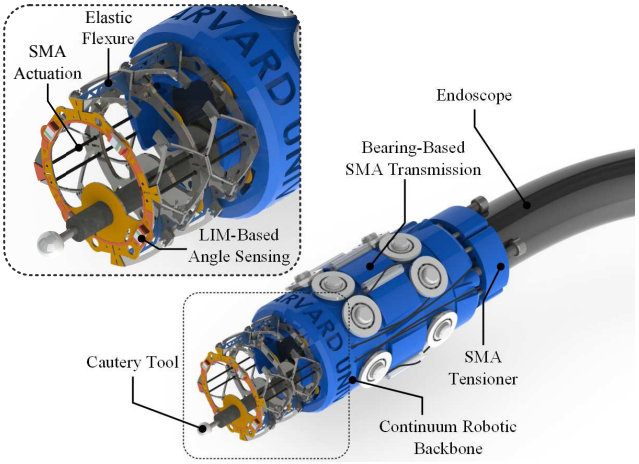

Fig. 1: Rendering of a distally-actuated 1 DoF modular wrist with callouts to important features. An articulating module interfaces with and deflects existing electrosurgical tools passed through the endoscope working port.

General trends in surgical endoscopy have pointed towards minimally-invasive applications in both diagnostic and therapeutic interventions that were previously impossible to perform. A burgeoning transendoscopic technique called endoscopic submucosal dissection (ESD) is being seen as a promising means of removing early-stage gastric neoplasia in a minimally-invasive way [6]. The technique involves the insertion of an endoscope or gastroscope through the mouth, navigating to the site of the tumor, and using a combination of forward-cutting and side-cutting bipolar cautery to resect and remove the diseased tissue from the submucosal space. Due to the technical and cognitive complexity involved, coupled with a reliance on surgical devices that are ill-suited for the task at hand, ESD has seen limited penetration into clinical practice. In addition, the unintuitive mapping between the endoscope controls and the distal dexterity required at the tip make ESD a prime candidate for robotic innovation.

*This material based on work supported by Defense Advanced Research Projects Agency (DARPA), A2P (Grant No. FA8650-15-C-7548). This work was also partially funded by the Wyss Institute for Biologically Inspired Engineering and the John A. Paulson School of Engineering and Applied Sciences at Harvard University.

J. Gafford is with the John A. Paulson School of Engineering and Applied Sciences at Harvard University, Cambridge, MA 02138 USA (jgafford@seas.harvard.edu).

T. Ranzani and S. Russo are with the John A. Paulson School of Engineering and Applied Sciences, Harvard University, Cambridge, MA 02138 USA, and the Wyss Institute for Biologically-Inspired Engineering, Harvard University, Boston, MA 02115 USA (tranzani, srusso@seas.harvard.edu).

H. Aihara and C. Thompson are with Brigham and Women's Hospital, Boston, MA 02115 USA (haihara, ccthompson@partners.org).

R. Wood and C. Walsh (corresponding author) are with the Faculty of the John A. Paulson School of Engineering and Applied Sciences at Harvard University, Cambridge, MA 02138 USA, and the Wyss Institute for Biologically-Inspired Engineering, Harvard University, Boston, MA 02115 USA (rwood, walsh@seas.harvard.edu).

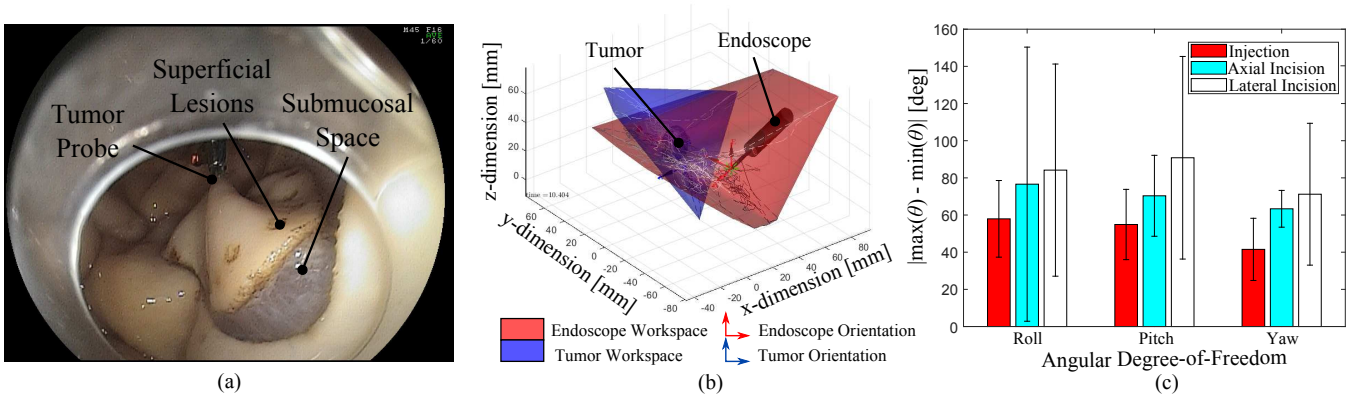

(a) (b) (c)

Fig. 2: (a) Endoscopic view of an ESD site, where the EM probe can be seen clipped into the tumor site, (b) re-constructed workspace of the tumor and the endoscope, and (c) results of meta-analyses showing dexterity achieved by the endoscope during each subtask.

Several groups have explored robotic solutions to the technical challenges imposed by ESD and endoscopic procedures in general [7]–[12]. Such implementations typically feature stand-alone robotic systems or roboticized 'add-ons' (overtubes or endcaps) to existing endoscopic equipment, where proximal actuator packages control distal end-effectors passed through the endoscope's working ports or around the outside. While these systems demonstrate endoscopic applications of robotics, proximal actuation schemes can limit modularity, clutter the surgical arena, and preclude the systems from single-use, disposable price points due to the intimate mechanical coupling between expensive proximal actuation systems and distal mechanisms.

In this paper, we present a robotic end-cap that interfaces with commercial endoscopes to provide distal dexterity to existing cautery devices passed through the endoscopic working channel, as shown in Fig. 1. A composite manufacturing process (PCMEMS) was used to monolithically fabricate the complex articulating structure, greatly reducing assembly requirements. Embedded orientation sensing is implemented on-board using distributed emitter/detector pairs and the principle of light intensity modulation. The actuation transmission system leverages shape memory alloy (SMA) technology and is fully contained within a 1"-long end cap that can be mounted on the distal end of the endoscope, making the system fully deployable with no proximal component. The low cost of raw materials coupled with batch manufacturing processes results in a potentially disposable system.

Section II presents the results of empirical clinical studies implemented to obtain workspace/range-of-motion and force data to characterize the procedure and generate task-specific system functional requirements. These clinical parameters were used to inform the creation of functional requirements for the proposed system, and Section III discusses system design, modeling and optimization based on these requirements. Section IV presents the subsystem-level manufacturing processes, as well as integration and validation of the system at a proof-of-concept level.

II. Clinical Parameterization

When designing robotic systems for task-specific applications, it is important to understand (1) the workspace that the system is required to cover, and (2) the forces which will be encountered and must be generated by the system. Given the relative sparsity of ESD-specific clinical data in literature (although briefly addressed in [13]), we employed an experimental approach to define these clinical requirements to inform the data-driven design process of a specialized robotic module tailored specifically for ESD.

A. Workspace Analysis

In collaboration with an experienced endoscopist at Brigham and Women's Hospital (Boston, MA), we used electromagnetic (EM) motion tracking technology to capture the position and orientation of the endoscope and a simulated tumor during three complete ESDs, as shown in Fig. 2 (a). Procedures were performed *ex vivo* on a porcine stomach in a clinical laboratory setting. One EM probe was fastened to the endoscope tip, and another was clipped into the location of the simulated tumor, enabling 6-DoF motion data to be captured simultaneously from the tumor and the endoscope tip at a rate of 1 kHz. Motion and orientation data were parsed based on the subtask which they represent to characterize three primary phases of ESD: (1) liquid injection for tumor liftoff, (2) axial (forward-cutting) incision for hole creation, and (3) lateral (side-cutting) incision for tumor resection. Resulting data were filtered using a combined Sauvitsky-Golay/Median filter to remove noise induced by electrosurgical pulses.

A representative workspace reconstruction of the lateral incision process is shown in Fig. 2 (b). Lateral incision requires the largest workspace as it is the most difficult maneuver to perform in ESD, often requiring significant dexterity to create and 'sweep out' the submucosal space beneath the tumor.

Meta-analyses of each subtask are shown in Fig. 2 (c), where for each subtask (injection, axial incision and lateral incision), n = 8, 3, and 5, respectively. We see that the average angular dexterity required for lateral incision is around 90.3 ± 50.4 degrees. The large error in the lateral incision subtask is due to a retroflexion event wherein the endoscopist had to deflect the scope nearly 180 degrees to access the distal section of the tumor. If this event is

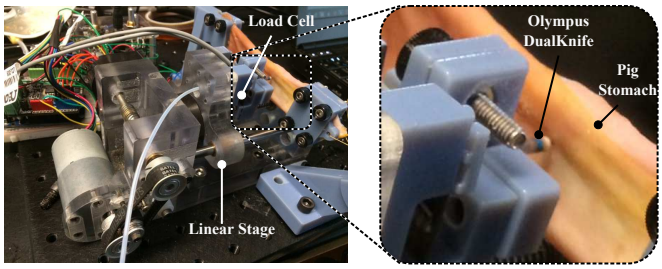

Fig. 3: Interaction force measurement system for measuring forces encountered during electrocautery.

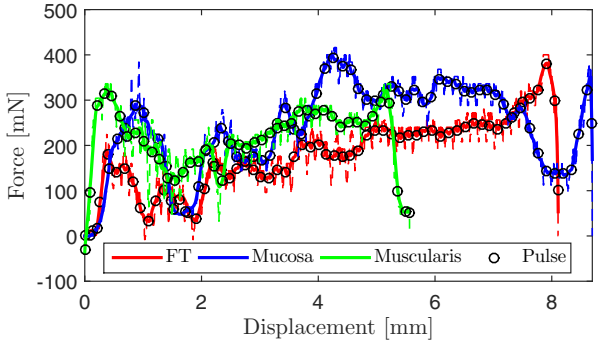

Fig. 4: Interaction forces between Olympus DualKnife bipolar cautery system and various layers within a porcine stomach. Circular markers denote cautery pulse events.

excluded, the average angular dexterity required for the lateral incision is 66.4 ± 20.3 degrees. Therefore, as a first step towards capability augmentation, we will seek to provide 60 additional degrees of angular deflection with this system.

B. Force Analysis

In developing a task-specific robotic system, it is also beneficial to have a thorough understanding of the types and magnitudes of forces that will be encountered. To determine these experimentally, a system was built (shown in Fig. 3) that enabled us to measure interaction forces between commercial electrosurgical equipment and pre-tensioned tissue specimens during a resection event. A bipolar cautery device (Olympus DualKnife) is clamped onto a load cell (LCL-005, Omega Engineering) which is attached to a leadscrew-based linear stage with sub-μm position encoding. The tissue specimen is clamped and pre-tensioned distal to the surgical tool. The tool is advanced into the specimen and pulsed simultaneously, and data (force and displacement) is captured at a rate 500Hz until the tool has fully penetrated through the tissue specimen.

The results of tests performed on three different porcine stomach tissue morphologies (full thickness, mucosal layer, and muscularis layer) are shown in Fig. 4. We see in each case a maximum axial force of around 300-400 mN is required to fully perforate the tissue. Therefore, any system we design for this purpose must be able to generate at least 400 mN of force for electrocautery.

III. System Design

Given the results of the clinical parameterization study, a robotic system was designed to satisfy the aforementioned

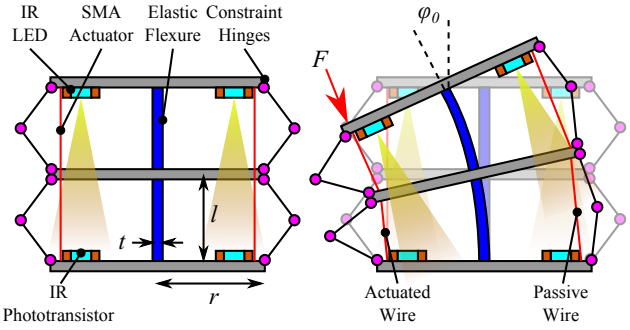

Fig. 5: Conceptual illustration of flexural backbone operation with integrated optical angle sensing. Passive flexure-based rotary joints (pink circles) facilitate assembly and prevent axial torsion.

requirements. An illustration of the articulating module is shown in Fig. 5. Similar to many other tendon-driven continuum systems, various disk-shaped spacers are equally separated axially along an elastic mechanism. Tendons pass through intermediate spacers and terminate on the distal-most spacer, such that when a tensile force is applied to the tendon, a moment is created about the elastic mechanism, thereby causing the structure to bend.

The system proposed herein differs in a few ways from previous tendon-based continuum systems. The system will be mounted on an endoscope so there must be an unobstructed bore, and as a result, the elastic mechanism cannot be placed in the geometric center of the spacer disks, but rather along the outside. We also want to minimize the system's imposition into the endoscope's vision system, thereby introducing a trade-off between footprint minimization and system robustness. In addition, integrated infrared LEDs and phototransistors can be mounted on subsequent spacer disks, enabling distributed angle sensing by light intensity modulation (LIM) [14].

In order to develop a fully modular, compact, distally-mounted system with no proximal component, shape memory alloy (SMA) was pursued as the method of actuation due to its high energy density, compactness, and relatively simple (on/off) control. Limitations of SMA actuation were heavily considered and deemed to be insubstantial for this application. For example, as the lateral incision process is relatively slow, actuator bandwidth is not a major concern. The use of very thin SMA wire results in very localized thermal dissipation which can be easily insulated. Controllability is beyond the scope of this paper, although we do present embedded orientation sensors that can be used for closed-loop feedback control [15].

The following section presents geometric parameter selection via brute force optimization methods, as well as a general model (nonlinear and linear) for LIM-based angle sensing for tendon-driven continuum or flexure-based robotic structures.

A. Geometric Optimization of Articulating Module

We employ a brute force optimization approach to determine flexure stiffness parameter t and input force F required to (a) generate the required dexterity (deflection angle ϕ_0 according to Fig. 5) and (b) ensure that the

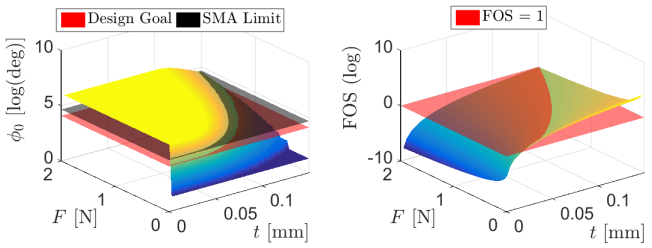

Fig. 6: (a) Parametric map of angular dexterity $2\phi_0$ as a function of input force F and flexure thickness t, where the red plane shows the design goal and the black plane shows the SMA stroke limit, (b) parametric map of the mechanical factor-of-safety as a function of F and t where the red plane shows FOS=1.

flexure remains within its elastic limit over the entire stroke. Other parameters, such as radius r and flexure width w, are constrained by the functional requirements of the system (i.e. the system cannot add more than 2mm to the outer diameter of the endoscope). To determine $\phi_0(F,t)$, we use a large-deflection model [16] for thin beam bending given a pure moment and a fixed end condition:

$$l = \frac{2EI}{NFr}\int_0^{\phi_0} \frac{d\phi}{\sqrt{\sin\phi_0 - \sin\phi}} \tag{1}$$

where l is the length of the flexure in a single articulating module, N is the number of articulating modules stacked in series, E is the Young's Modulus of the flexure material, and I is the second moment of area. In Equation (1), the integral was solved numerically to compute $\phi_0(F,t)$ for some combination of F and t. Due to symmetry and the use of antagonistic actuation, we can generate $\pm\phi_0$ for an overall angular deflection of $2\phi_0$ to satisfy the functional requirement. Parametric surfaces resulting from this optimization are shown in Fig. 6 for $N = 2$. Fig. 6 (a) shows the (log) angular dexterity as a function of input force F and flexure thickness t. The red plane shows the design requirement, and the black plane shows the SMA upper-limit (as the actuator is inherently stroke-limited). The design goal is to find a combination that exists on the parametric landscape above the red plane but acknowledging that stroke performance is limited by the black plane. A flexure thickness of 75 μm and an actuation force of 1 N or above satisfies this requirement. We also want to ensure that the elastic flexure remains within its elastic limits by satisfying the following equation for mechanical factor-of-safety (FOS > 1):

$$\text{FOS} = \frac{4NI\sigma_y}{Frt} \tag{2}$$

where σ_y is the yield stress. Fig. 7 (b) shows the (log) FOS, where the red plane shows an FOS of 1. We see that the chosen combination results in FOS>1, so both conditions are satisfied.

B. Sensor Modeling

In previous work [14] we demonstrated the use of discrete, distally-mounted LEDs and phototransistors to sense deflection (or force) in a structure. We showed that the irradiance striking the phototransistor (PT) from a point-source LED model falls off with the square of the distance separating the LED from the PT. In this implementation, as shown in Fig. 5, misalignment between the two axes as the backbone deforms introduces a cosine term, resulting in the following equation for irradiance E_{PT} striking the phototransistor:

$$E_{PT} = \cos(\phi_0)\frac{I_{LED}}{(h - r\sin(\phi_0))^2} \tag{3}$$

where I_{LED} is the radiant intensity from the LED and $h = Nl$ is the spacing between the LED and PT. From this, we can calculate the phototransistor collector current i_{PT} as a function of the irradiance:

$$i_{PT} = \exp\left(\alpha\log(E_{PT}) + \beta\right) \tag{4}$$

where α and β are fit constants.

It is possible to linearize this function about $\phi = 0$ to obtain a simple calibration model relating phototransistor current i_{PT} to angular deflection ϕ_0:

$$i_{PT} = i_{PT}(\phi_0)|_{\phi_0=0} + \left.\frac{\partial i_{PT}(\phi_0)}{\partial\phi_0}\right|_{\phi_0=0}(\phi) = b + m\phi_0 \tag{5}$$

$$b = \exp\left(\alpha\log\left(\frac{I_{LED}}{h^2}\right) + \beta\right) \tag{6}$$

$$m = \frac{\alpha h^2\left(\frac{2I_{LED}r}{h^3}\right)\exp\left(\alpha\log\left(\frac{I_{LED}}{h^2}\right) + \beta\right)}{I_{LED}} \tag{7}$$

Numerical analysis shows that there exists less than 6% error between the full model and the linear simplification over the expected range-of-motion.

IV. Manufacturing and Validation

An overview of the fabricated system and its subsystems is shown in Fig. 7. The following section will discuss the manufacturing processes used to fabricate each subsystem and present preliminary results from both a subsystem and integrated system perspective.

A. Articulating Module

The articulating exoskeleton module was fabricated using PCMEMS [17], [18]. The layup consists of 15 layers of material, including four layers of 75 μm 304 stainless steel for the structural layers, two layers of 25 μm Kapton polyimide for the flexure-based assembly layers, seven layers of DuPont FR0100 acrylic sheet adhesive, and two layers of 25 μm Kapton with an 18 μm Copper cladding layer. Each layer is machined individually using a diode-pumped solid-state (DPSS) laser, and all 15 layers are laminated together in a heat press. Preliminary release cuts are made to free the guided assembly Sarrus linkages, as shown in Fig. 8, and the system is placed in a pin-actuated alignment jig (Fig. 9) where thumbscrew-driven push pins provide the actuation required for self-folding and assembly. In addition

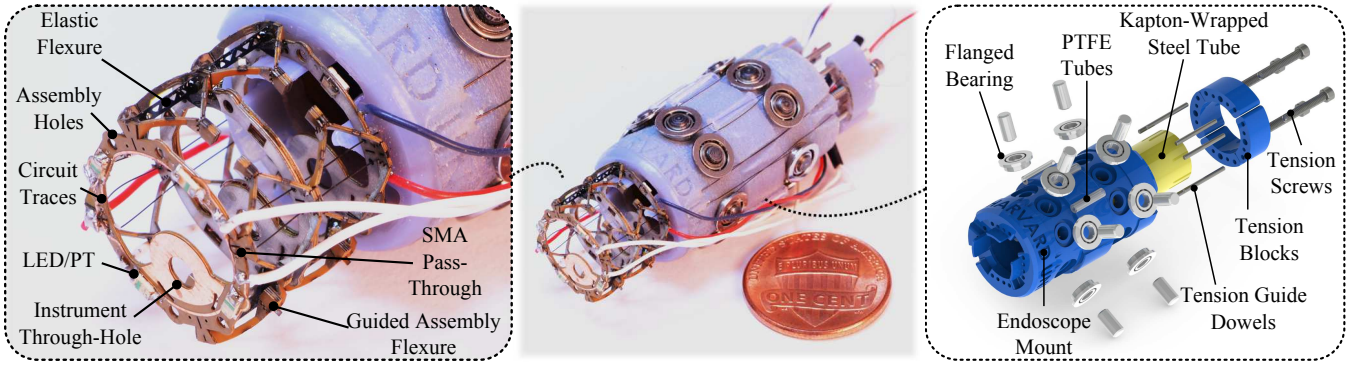

Fig. 7: System overview, showing (left) a detail of two serial articulating modules fabricated via PCMEMS and callouts to important features, (middle) integrated system with a US penny for scale, and (right) exploded detail of the SMA transmission mechanism.

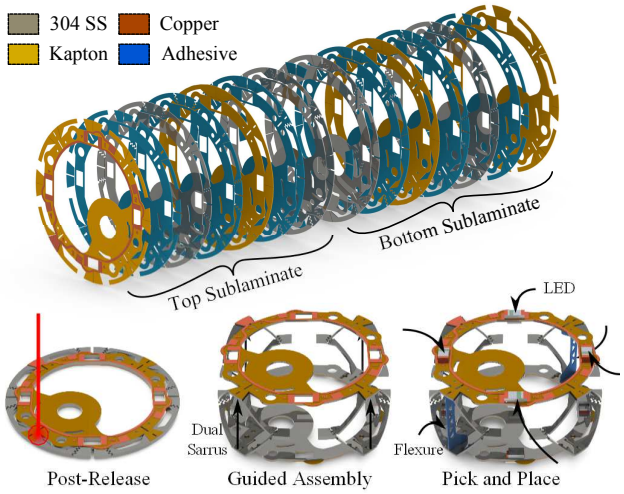

Fig. 8: (top) Exploded view of the 15-layer laminate, and (bottom from left) laser-machining to release assembly sarrus linkages, guided assembly of the articulating exoskeleton, and pick-and-place of flexures, phototransistors and LEDs (assembly scaffold omitted for clarity). Refer to multimedia extension for an illustration of the process.

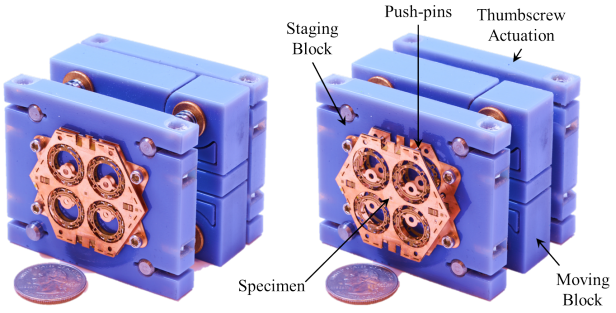

Fig. 9: Thumbscrew-actuated staging and assembly jig for the assembly scaffold, where (left) shows the flat PCMEMS structure and (right) shows the 'popped-up' structure.

to guiding the assembly, these Sarrus linkages also provide an integrated 'mechanical limit' that prevents over-deflection of the structure. Two 75 μm tempered spring steel flexures are placed into slots in the structure and epoxied into place, and the entire laminate is once again machined in the DPSS laser to release the structure from the surrounding hexagonal alignment scaffold. LEDs and PTs are press-fitted into their respective windows in the structure and reflow soldered to complete assembly.

B. SMA Transmission Module

In order to generate the required stroke from the SMA actuator (3mm), a 150mm long actuator wire is required (assuming 4% contraction and accounting for the 'doubling back' of the SMA which halves the stroke but doubles the force output). To keep the system compact, a transmission module was designed featuring low-friction sliding surfaces and flanged ball bearings, allowing the wire to be 'wound' back and forth several times, thereby significantly driving down the overall footprint of the entire system. An image of this transmission module is shown in Fig. 7 (right). The SMA is fed into a transmission module from the SMA anchors on the articulating exoskeleton, wound through a series of bearing surfaces, and terminated at tensioning blocks that are leadscrew-driven, enabling independent adjustable pre-tensioning of each actuator.

C. Signal Conditioning and Sensor Calibration

Due to the wide spectral bandwidth of the phototransistor's response (400-1100 nm), special considerations must be made in developing signal conditioning infrastructures such that DC-level ambient signals are not amplified. An AC-coupled excitation circuit based around an astable oscillator for the emitter side was implemented, pulsing the IR LEDs at a rate of 8 kHz. The collector-side is filtered and amplified with an active band-pass filter centered at 8 kHz. This scheme is described in more detail in [14]. Such an implementation renders the sensing system impervious to ambient conditions. It is possible that cross-talk between sensors could affect individual sensor readings as there is no optical isolation between sensor pairs (aside from an axial offset). A robust solution would be to pulse the LEDs in each sensor pair at a different frequency and band-passing the respective phototransistor output centered to the LED frequency, although this would require more wires as each LED would require its own excitation lead. For the purpose of this paper, cross-talk is assumed to be suitably accounted for in calibration.

The angle sensor was calibrated statically by hanging weights from the SMA anchors, measuring the angle and recording the sensor outputs. The calibration curve is shown in Fig. 10. Pairs of sensors oppose each-other, offering the opportunity to perform differential measurements to eliminate

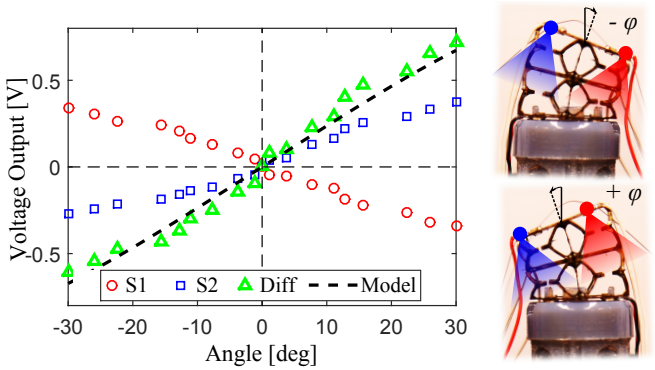

Fig. 10: LIM-based angle sensor calibration results compared to the predictive model. Images show how redundant sensors can be used for differential measurements, eliminating common-mode noise. Refer to multimedia extension for real-time video.

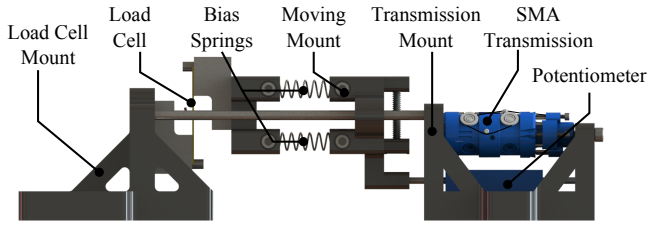

Fig. 11: SMA characterization platform with callouts to important features.

common-mode sources of noise that were not adequately filtered in signal conditioning (such as local heating due to SMA). We can see that the actual sensor implementation behaves very closely to that predicted by the model.

D. SMA Characterization

To better understand the force and stroke capabilities of the SMA wire under ideal conditions, a characterization platform was developed, as shown in Fig. 11. The platform consists of a stationary mount where the SMA transmission module can be dropped in. The SMA is routed through a moving platform which glides smoothly on lubricated steel shafts to constrain motion to the actuation axis. A low-friction slide potentiometer tracks the location of the moving platform. The moving platform is coupled to a stationary load cell (LCL-005, Omega Engineering) via extension springs whose pre-tension can be modified by adjusting the distance between the load cell mount and transmission mount.

Using the final transmission design, 0.006" (152 μm) Flexinol^{TM} actuator wire (Dynalloy, Irvine, CA) was tested for its contraction properties under varying force biases. To activate the SMA, 360 mA of current was applied in the form of a 1/10 Hz square wave with 60% duty cycle, resulting in 6 seconds of heat-up time and 4 seconds of cool-down time. Data were collected using USB-6002 DAQ (National Instruments) with a 1 kHz sample rate. The results are shown in Fig. 12 (a). We observe diminishing returns after a 1.5N bias force, however we see that 1N bias is insufficient to properly pre-tension the wire. Some of the stroke is lost to slack in the system, thereby compromising performance and contraction efficiency. As a result, 1.5N of pre-tension is

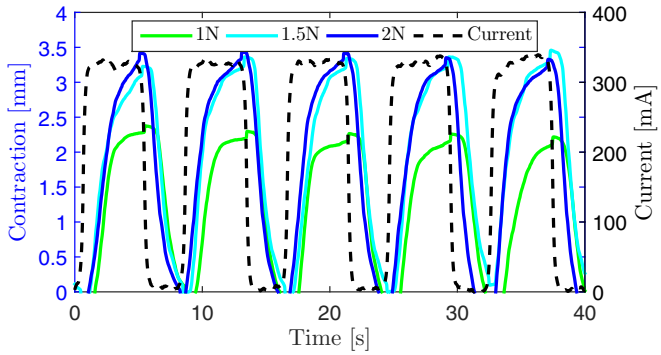

(a)

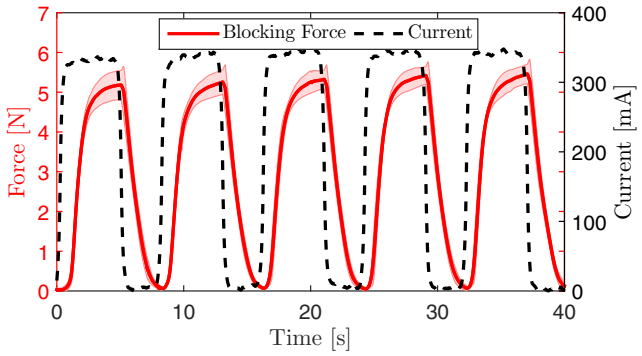

(b)

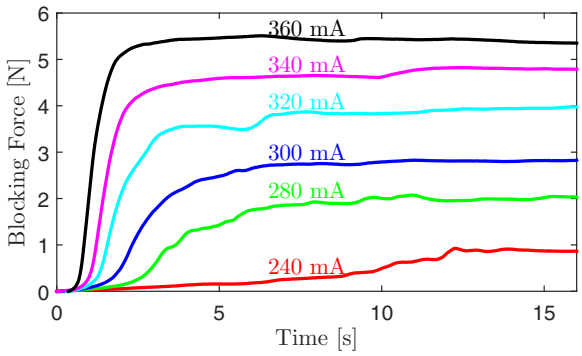

(c)

Fig. 12: Results of SMA characterizatiton, showing (a) the contraction profile as a function of time for various pre-tension biases, (b) blocking force profile as a function of time (shaded area shows standard deviation for $n = 5$ runs), and (c) blocking force evolution as a function of input current.

sufficient for high-efficiency operation. We also observe that the SMA contracts over 3mm with adequate pre-tension.

We also want to characterize the blocking force capabilities of the SMA (that is, the reaction force which fully prevents the SMA from contracting) to understand the force output capabilities of the system. By coupling the SMA directly to the load cell (i.e. bypassing the bias springs such that there is no contraction), pre-tensioning to 1.5N, and providing the same current profile as before, a force profile as shown in Fig. 12 (b) is achieved. We observe that the SMA is able to provide over 5N of contraction force *in addition to* the force required to overcome the bias (that is, the actuator can produce 5N of usable force). The inherent stroke limitation prevents the SMA from damaging the articulating structure which only requires 1N to deform, as designed. As such,

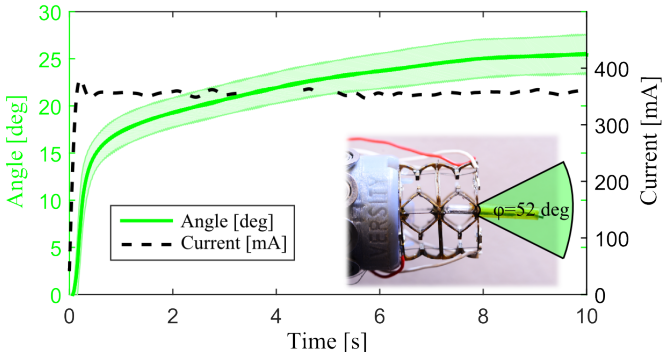

Fig. 13: System actuated over a positive angle and the resulting on-board sensor measurements. Inset shows unactuated system and system at the extreme of actuation. Refer to multimedia extension for real-time video.

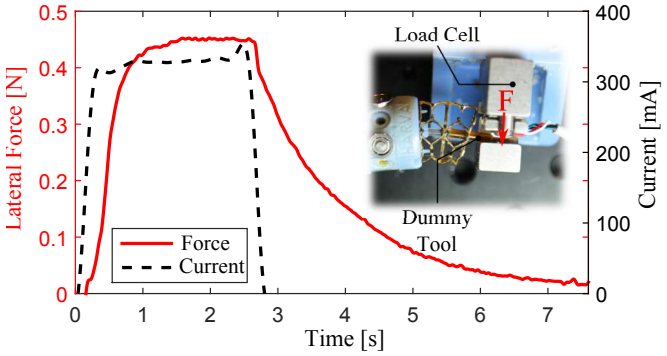

Fig. 14: Lateral force profile for a step input in current.

4N is left over for bending the cautery tool to withstand tissue reaction forces. Finally, Fig. 12 (c) shows how the force develops over time as a function of input current given a step input, lending some insight into the system bandwidth.

E. Integrated System Validation

The articulating module was attached to the transmission module, and two 140 mm long, 0.006" diameter actuator wires were routed around the bearing transmission and through the articulating module. The individual tensioner blocks were tightened up to about mid-stroke for each SMA (allowing the opposing SMA to 'relax' as the actuated SMA contracts). A step current of 360 mA was applied for 10 seconds, and the on-board sensor readings were collected at a rate of 500 Hz. The final deformed shape was measured and compared to the sensor readings. Fig. 13 shows the differential on-board sensor readings over a positive actuation angle given step input currents. We observe that the system is able to achieve 25.5 ± 2.25 degrees of motion for positive and negative angles, leading to a total of 51 ± 4.5 degrees, and the sensors were able to resolve this deflection. It was observed that some stroke was lost in deforming the distal-most spacer disk, so future work will focus on making the system more robust by using thicker layers of material.

It was also observed that the elasticity of the integrated flexural element was not sufficient to pre-bias the SMAs (i.e., when one SMA had actuated and deformed the structure, in order to straighten the structure out again by returning the

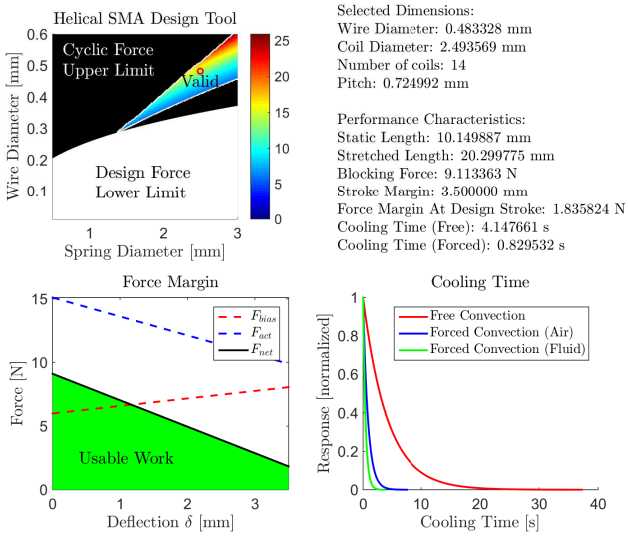

Fig. 15: Helical SMA design tool for hypothetical analysis: (clockwise from top left) valid solution space given design constraints (where marker denotes selected configuration), design and performance characteristics, thermodynamic behavior, and force margin over design stroke.

actuated wire to its untwinned martensitic state, the antagonistic actuator had to be actuated to provide the necessary bias force). Future design iterations will focus on optimizing the trade-off between the flexure's ability to provide both the required dexterity as well as the passive biasing force the SMAs need to relax. From a controllability perspective, this is beneficial, as the structure would passively straighten.

The system was also tested for its lateral force generation capabilities. A mock instrument (silicone tubing with 0.020" nitinol tube inside) was fed through the instrument port, and the system was actuated against a load cell. A pulse of 360 mA was provided to heat the SMA on one side, thereby causing it to actuate against the load cell, and the reaction force was captured at a rate of 500 Hz. The resulting force profile shown in Fig. 14 shows that the system can generate 450 mN of lateral force when actuated and sustain this force for several seconds, thereby satisfying the force requirement.

F. Helical SMA Actuation: Theoretical Analysis

The performance of the current system is limited in large part by the stroke, high stiffness (which makes pre-tensioning a challenge in antagonistic systems) and bandwidth limitations of the SMA wire actuators. In the interest of improving stroke and stiffness tunability characteristics, a preliminary analysis was performed to determine the geometric properties required from a spring-wound helical SMA actuator that would improve the stroke while maintaining similar blocking force characteristics. A design tool was implemented in MATLAB using constitutive equations found in [19] (omitted here for brevity), to generate a parametric space of the potential net force output as a function of reasonable spring geometrical parameters (wire diameter d and coil outer diameter D) and user-inputted parameters (design force F and stroke δ). An example parametric map is shown in Fig. 15 (top left), where valid geometrical solutions are those

that generate actuation forces which (1) meet or exceed the design force requirements, and (2) induce shear stresses in the SMA which are less than the cyclic limit of the material. Note that more sophisticated models incorporate martensitic de-twinning phenomena but these effects are assumed negligible for sub-critical shear stress levels [20]. For the configuration of d = 0.5mm and D = 2.5mm, Fig. 15 (lower left) demonstrates a usable work range over about 3.5mm of stroke, thereby exceeding the stroke requirements of the current system and generating 70 degrees of deflection.

The bandwidth is limited by the cooling time of the SMA which is a thermodynamic process that scales linearly with wire radius. Although it was determined from the application that circumferential incision is a low-bandwidth process, developing faster actuation methodologies will invariably improve system controllability. By implementing forced convection cooling, thermodynamic analyses (Fig. 15 (lower right)) show that cooling time can be sped up significantly, making >Hz bandwidth achievable [21].

V. Conclusion

In this paper, we present a fully-distal snap-on robotic module for endoscopic procedures. System design was informed by clinical parameters which were found experimentally. Integrated sensing and actuation provides fully modular capabilities, thereby obviating the need for proximal actuator packages and transmission mechanisms. The integrated system demonstrated the ability to provide 51 ± 4.5 degrees of angular dexterity and generate lateral forces of around 450 mN which is sufficient for cautery.

Future work will focus on increasing the stroke and packaging the actuators such that they are not exposed to biological tissue. As per the analysis provided in Section IV, spring-wound SMA actuators will be investigated under the hypothesis that greater stroke and stiffness tunability is achievable. We will also explore alternative actuation strategies (electrostatic, hydraulic/pneumatic) in parallel. We will investigate integration with soft materials to encapsulate the articulating structure for added robustness. We will also explore alternative materials (i.e. superelastic) for the flexure mechanism, as well as multi-DoF articulation by rotating subsequent articulating modules with respect to eachother. The system will be adapted to a commercially-available endoscope, and we will investigate its efficacy *ex vivo* by collaborating with expert endoscopists to perform an *ex-vivo* ESD on a porcine stomach. We will also investigate closed-loop control using on-board sensor data to implement lower-level control with the ultimate goal of subtask automation.

References

[1] P. E. Dupont, J. Lock, B. Itkowitz, and E. Butler, "Design and Control of Concentric-Tube Robots," *IEEE Transactions on Robotics*, vol. 26, no. 2, pp. 209–225, 2010.

[2] J. S. Schneider, J. Burgner, R. J. Webster, and P. T. Russell, "Robotic surgery for the sinuses and skull base: what are the possibilities and what are the obstacles?," *Current opinion in otolaryngology & head and neck surgery*, vol. 21, no. 1, pp. 11–6, 2013.

[3] K. Weaver, R. Webster III, P. Swaney, J. Burgner, P. Russel, H. Gilbert, J. Bekeny, and R. Hendrick, "The Use of Teleoperated Concentric-Tube Robots for Transsphenoidal Parasellar Surgery.," *Journal of Neurological Surgery, Part B.*, vol. 74, no. A123, 2013.

[4] A. Bajo, L. M. Dharamsi, J. L. Netterville, C. G. Garrett, and N. Simaan, "Robotic-Assisted Micro-Surgery of the Throat : the Trans-Nasal Approach," *IEEE International Conference on Robotics and Automation*, pp. 232–238, 2013.

[5] T. Ranzani, M. Cianchetti, G. Gerboni, I. Falco, and A. Menciassi, "A soft modular manipulator for minimally invasive surgery: Design and characterization of a single module," *Robotics, IEEE Transactions on*, vol. 32, pp. 187–200, Feb 2016.

[6] J. T. Maple, B. K. Abu Dayyeh, S. S. Chauhan, J. H. Hwang, S. Komanduri, M. Manfredi, V. Konda, F. M. Murad, U. D. Siddiqui, and S. Banerjee, "Endoscopic submucosal dissection," *Gastrointestinal Endoscopy*, pp. 1–15, 2015.

[7] K. Kume, N. Sakai, and T. Goto, "Development of a novel endoscopic manipulation system : the Endoscopic Operation Robot ver . 3," *Endoscopy*, vol. 47, pp. 815–819, 2015.

[8] R. Nakadate, S. Nakamura, T. Moriyama, H. Kenmotsu, S. Oguri, J. Arata, M. Uemura, K. Ohuchida, T. Akahoshi, T. Ikeda, M. Hashizume, M. Hashizume, and M. Initiatives, "Gastric endoscopic submucosal dissection using novel 2.6-mm articulating devices: an ex vivo comparative and in vivo feasibility study.," *Endoscopy*, pp. 820–824, 2015.

[9] M. F. Traeger, D. B. Roppenecker, M. R. Leininger, F. Schnoes, and T. C. Lueth, "Design of a spine-inspired kinematic for the guidance of flexible instruments in minimally invasive surgery," *2014 IEEE/RSJ International Conference on Intelligent Robots and Systems*, no. Iros, pp. 1322–1327, 2014.

[10] G. P. Mylonas, V. Vitiello, T. P. Cundy, A. Darzi, and G.-z. Yang, "CYCLOPS : A Versatile Robotic Tool for Bimanual Single-Access and Natural-Orifice Endoscopic Surgery," *IEEE International Conference on Robotics and Automation*, pp. 2436–2442, 2014.

[11] J. Ruiter, E. Rozeboom, M. Van Der Voort, M. Bonnema, and I. Broeders, "Design and evaluation of robotic steering of a flexible endoscope," *Proceedings of the IEEE RAS and EMBS International Conference on Biomedical Robotics and Biomechatronics*, pp. 761–767, 2012.

[12] S. J. Phee, N. Reddy, P. W. Chiu, P. Rebala, G. V. Rao, Z. Wang, Z. Sun, J. Y. Wong, and K. Ho, "Robot-Assisted Endoscopic Submucosal Dissection Is Effective in Treating Patients With Early-Stage Gastric Neoplasia," *Clinical Gastroenterology and Hepatology*, vol. 10, no. 10, pp. 1117–1121, 2012.

[13] D. B. Roppenecker, A. Meining, G. Horst, H. Ulbrich, and T. C. Lueth, "Interdisciplinary development of a Single-Port Robot," *International Conference on Robotics and Biomimetics*, pp. 612–617, 2012.

[14] J. B. Gafford, S. Member, R. J. Wood, and C. J. Walsh, "Self-Assembling, Low-Cost, and Modular mm-Scale Force Sensor," *IEEE Sensors Journal*, vol. 16, no. 1, pp. 69–76, 2016.

[15] N. Kha and K. Ahn, "Position Control of Shape Memory Alloy Actuators by Using Self Tuning Fuzzy PID Controller," *IEEE Conference on Industrial Electronics and Applications*, pp. 1–5, 2006.

[16] T. Beléndez, C. Neipp, and A. Beléndez, "Large and small deflections of a cantilever beam," *European Journal of Physics*, vol. 23, no. 3, pp. 371–379, 2002.

[17] P. S. Sreetharan, J. P. Whitney, M. D. Strauss, and R. J. Wood, "Monolithic fabrication of millimeter-scale machines," *Journal of Micromechanics and Microengineering*, vol. 22, no. 5, p. 055027, 2012.

[18] J. P. Whitney, P. S. Sreetharan, K. Y. Ma, and R. J. Wood, "Pop-up book MEMS," *Journal of Micromechanics and Microengineering*, vol. 21, no. 11, p. 115021, 2011.

[19] B. Holschuh and D. Newman, "Low spring index, large displacement shape memory alloy (SMA) coil actuators for use in macro- and micro-systems," *Proc. of SPIE*, vol. 8975, p. 897505, 2014.

[20] S. Yates and A. Kalamkarov, "Experimental Study of Helical Shape Memory Alloy Actuators: Effects of Design and Operating Parameters on Thermal Transients and Stroke," *Metals*, vol. 3, no. 1, pp. 123–149, 2013.

[21] Y. Tadesse, N. Thayer, and S. Priya, "Tailoring the Response Time of Shape Memory Alloy Wires through Active Cooling and Pre-stress," *Journal of Intelligent Material Systems and Structures*, vol. 21, no. 1, pp. 19–40, 2010.